The capability of very high-resolution satellite imagery for plot-level early wheat stem rust disease detection, monitoring, and phenotyping in Ethiopia

Gerald Blasch

g.blasch@cgiar.org

International Maize and Wheat Improvement Center

Ashenafi Gemechu

Debre Zeit Agricultural Research Center

Yoseph Alemayehu

International Maize and Wheat Improvement Center

Adama Ndour

International Maize and Wheat Improvement Center

Pablo Olivera Firpo

United States Department of Agriculture

Andries Potgieter

University of Queensland

David P. Hodson

International Maize and Wheat Improvement Center

Article

Keywords:

Posted Date: February 12th, 2026

DOI: https://doi.org/10.21203/rs.3.rs-7652033/v1

Additional Declarations: No competing interests reported.

The capability of very high-resolution satellite imagery for plot-level early wheat stem rust disease detection, monitoring, and phenotyping in Ethiopia

Gerald Blasch[1*], Ashenafi Gemechu[2], Yoseph Alemayehu[3], Adama Ndour[3], Pablo Olivera Firpo[4], Andries Potgieter[5], David P. Hodson[6]

[1] International Maize and Wheat Improvement Center (CIMMYT), Texcoco, Mexico
[2] Debre Zeit Agricultural Research Center (DZARC), Debre Zeit, Ethiopia
[3] International Maize and Wheat Improvement Center (CIMMYT), Addis Ababa, Ethiopia
[4] United States Department of Agriculture, St. Paul, MN, United States
[5] University of Queensland, Brisbane, Australia
[6] International Maize and Wheat Improvement Center (CIMMYT), Kathmandu, Nepal

Correspondence*: Gerald Blasch; g.blasch@cgiar.org

Abstract:

Very high-resolution satellites (VHRS) have potential for early crop disease detection and enhanced food security. The capability of multispectral SkySat and Pleiades-Neo imagery for early detection and monitoring was assessed for wheat stem rust (SR) at the plot level. In randomized trials with contrasting fungicide and irrigation treatments, six bread wheat varieties with differing SR susceptibility were monitored using VHRS. 113 multispectral features were evaluated for their association with SR progression and associated yield loss. Several features demonstrated moderate to strong correlations with SR disease levels. Across early disease stages (healthy-mild-moderate), spectral sensitivity was dominated by Blue (B)-based features, with Red-Blue (R-B) and Green-Blue (G-B) two-band features at mild and moderate levels, respectively. During late stages (severely-fully diseased), spectral sensitivity was driven by R-based features (e.g., R-B, R-G on both sensors) and by Deep Blue (DB), Red-Edge-DB (RE-DB), and R-DB combinations on Pleiades-Neo. Early SR detection under moderate disease pressure was possible using ratio (RSI) and normalized difference (NDSI) spectral indices with B-G combinations. Key SkySat features such as RSI(NIR,B), RSI(R,B), and RSI(G,B) were sensitive across scenarios. This work delivers the first VHRS-based SR detection, advancing monitoring from plot to regional scales.

Introduction

Transboundary pathogens are increasingly threatening global wheat production, with serious implications on food security [1,2]. Wheat stem rust (SR), stripe (yellow) rust (YR), and leaf rust (LR) are some of the most damaging, foliar wheat diseases caused by airborne fungal pathogens [3,4]. These pathogens are very destructive, highly variable, and very mobile [5–7]. Wheat rusts can cause epidemics on a vast scale, with estimated global production and economic losses of 15 million tons per year, a value of $2.9 billion [8]. With climate change and globalization, wheat disease outbreaks are likely to exacerbate in terms of increased geographical extent, frequency, and severity [9–11].

Wheat SR is considered the most aggressive of all wheat rusts, capable of causing 100% crop loss within weeks [3,12]. Historically, devastating SR epidemics have occurred in all wheat growing continents [13,14]. After effective control for nearly six decades, SR is re-emerging as a disease of concern. SR is returning to Europe [15–18], and highly virulent strains (Ug99) have been reported in South Asia for the first time [19]. Ethiopia, the largest wheat producer in Sub-Saharan Africa, is a SR disease hot spot with recurrent epidemics [20,21] and plays a crucial role for SR dispersion between Africa and Asia [5,6,22].

Wheat SR is caused by the obligate pathogenic fungus *Puccinia graminis* f. sp. *tritici* (Pgt). It is characterised by dark reddish-brown pustules that contain thousands of urediniospores. The infection can appear on any aboveground, living wheat parts, principally on stems, leaf sheaths, and leaf surfaces, but also occasionally on spikes [23]. In late stages, urediniospores transform into black teliospores. Wheat's xylem tissue, which transports water and dissolved minerals from the roots to other plant parts, is harmed by SR. Decreased supply of water and nutrients weakens plant parts, leading to diversion of photosynthetic assimilates, decreased photosynthetic area, and ultimately to chlorotic and necrotic plant tissue of leaves and stem, as well as reduced grain size [24,25]. These physiological alterations affect the spectral properties of wheat at the plant and canopy level in terms of pigmentation (e.g., chlorophyll), moisture, and biomass. Several studies demonstrated that multispectral reflectance bands and crop growth-related vegetation indices (VIs) derived from satellite data can deliver valuable information on wheat susceptibility to other wheat diseases, suggesting earth observation suitability for wheat disease detection and monitoring [26–33].

Recent advances in sensor technology and data processing increased the spatial and temporal capability of satellite remote sensing (RS) to measure plant biophysical and biochemical properties of plant canopies at high precision in near-real-time over large areas. Very high-resolution satellite (VHRS) systems such as Pleiades-Neo [34] and SkySat [35] can provide sub-daily panchromatic and multispectral coverage with sub-meter and ~1 m spatial resolutions, respectively.

To support crop breeding, VHRS multispectral imaging can be a practical and efficient high-throughput phenotyping (HTP) tool, permitting automated monitoring of field trials across multiple geographies using uniform platforms and standardized protocols [36,37]. In recent decades several studies assessed the relationship of VHRS-derived spectral features, such as native spectral broad bands and VIs, with key physiological traits, such as biomass, yield, and disease severity, for wheat, maize, canola, and dry beans [38–42]. Although these studies confirmed the feasibility of VHRS high-throughput phenotyping, the utilization of such satellite solutions for plant breeding programs are still in their infancy.

For disease early warning, the time of sensing determines the effectiveness of satellite data. Early disease detection at earlier growth stages is important to prevent large scale disease outbreaks and epidemics. However, most satellite-based wheat disease and monitoring studies focus on the grain filling stage as the optimal time to map wheat diseases due to visible disease symptoms present on plant parts [27,28,30,31,43–47]. That allows mostly for assessing the disease extent and damage rather than surveilling the disease spread. In most cases, this time of sensing is too late for undertaking efficient disease control measures. However, recent research demonstrated that multispectral VHRS data can assess wheat rust severity at earlier growth stages such as booting and heading [42].

In general, YR symptoms, i.e., leaf infections, are clearer to observe at the canopy level than SR symptoms (predominantly stem infections). Therefore, research has focused on investigating the capability of multispectral satellite RS technology for YR detection [28,29,33,43,48–50], identification [27], and quantification [28,30,51]. A recent review on RS applications for wheat rust diseases [52] highlighted that literature regarding SR detection and monitoring did not exist; neither for using ground-based, airborne nor spaceborne sensors. The authors concluded that the reason for this might be that SR infections appear primarily on the wheat stem and subsequently cannot be detected at the canopy level by airborne (e.g., UAV) or satellite sensors. The appearance of initial SR symptoms in the middle to lowest levels of the crop canopy challenges the application of airborne and spaceborne RS, especially for presymptomatic and early-stage detection [53]. However, the SR impact on wheat canopy will increase with disease progression [42].

To the best of our knowledge, only two recent studies on wheat SR phenotyping or detection using remotely sensed data have addressed the clear knowledge gap thus far. For SR quantification including low disease severity levels, the spectral sensitivity of low-altitude hyperspectral imaging was demonstrated [54]. For the detection of co-occurring YR and SR, several spectral features were found with high assessment power at earlier crop growth stages from UAV and VHRS multispectral data, demonstrating the potential of upscaling rust detection from field trial plots to regional scale [42].

The capability of multispectral VHRS imagery, typified by SkySat and Pleiades-Neo, for HTP and early disease detection and monitoring is assessed by investigating the interaction between SR and wheat varieties at the plot level in terms of early detection, host plant response to SR, and associated yield. The objectives were to (i) characterize the progressive SR development and associated grain yield loss using traditional visual disease estimations; and (ii) assess the level of agreement of remotely sensed multispectral features with visual disease scores of SR symptoms from early to late disease stages, general disease progression, and grain yield. An exploratory analysis using broad-band physiological spectral indices in addition to native spectral bands and VIs was performed in combination with Pearson correlation analysis.

Materials and methods

Study site

The field experiment was carried out at the EIAR Debre Zeit Agricultural Research Center (DZARC; 8°44’N / 38°58’E; 1,900 m above sea level) from February to May 2023 during the agricultural off-season to avoid frequent cloud cover impeding satellite data acquisition. DZARC is located in the East Shewa zone (Ada’a district) of the Oromia Region, central highlands of Ethiopia (Figure 1). The average daily minimum and maximum temperatures are 8.9°C and 28.3°C, respectively, and the mean annual rainfall is 851 mm. A bimodal rain distribution pattern allows for a growing period of 61-120 days [55], whereby *Belg* rains occur between February and April (short rainy season) and *Meher* rains from June to September (long rainy season). Crop production is closely linked to the *Meher* season, with crops harvested between September and November. The predominant soil type is clayey soils (e.g., vertisols) [56]. Prevailing climatic conditions in the DZARC area are favorable for rust development in the rainy seasons, rendering wheat fields in this region highly susceptible to natural infection. As mitigation measure, the experiment was conducted during the dry season.

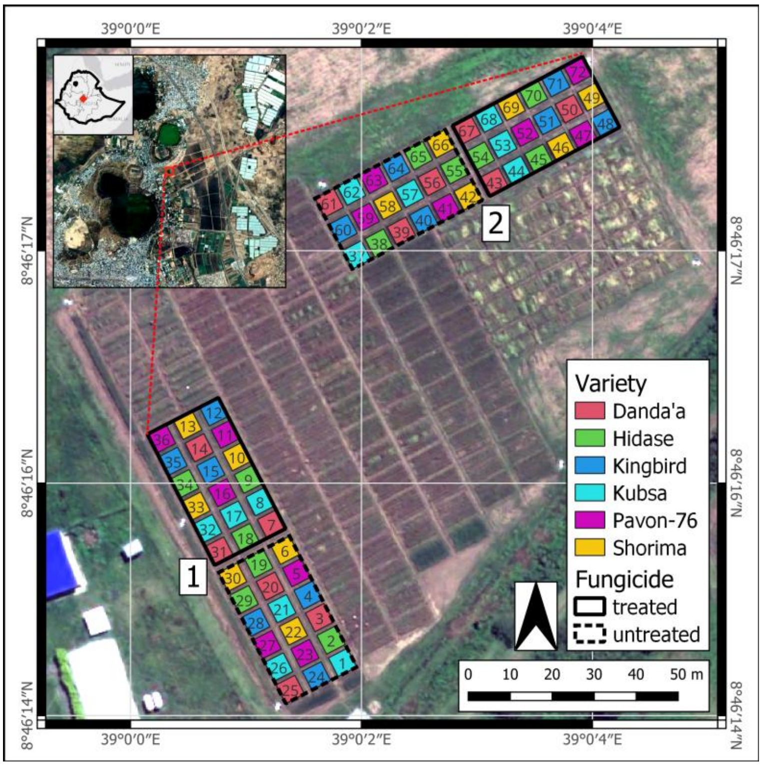

Figure 1. Location of the study site and illustration of the experimental setups: Trial 1 (1; weekly irrigation scheme) and Trial 2 (2; bi-weekly irrigation scheme) with treatment blocks related to disease control (solid line: fungicide application – treated; dashed line: without fungicide control – untreated) (experiment trials: Pleiades-Neo RGB image from 2023-05-06; study site: Google Satellite). Figure prepared using QGIS version 3.28.11-Firenze [57].

Plant material

For the experiment, six improved bread wheat varieties with varying levels of susceptibility to the present prevailing races of the SR pathogen were selected (Table 1). The varieties have been assessed for agronomic performance and resistance to SR in multiple locations and years across Ethiopia [58–61].

Table 1. Characteristics of selected wheat varieties.

Variety	**Origin**	**Release Year**	**SR Infection Response** [60]	**Farmers' Rating** [58]
Danda'a	EIAR-CIMMYT	2010	S-MS	very good to excellent
Hidase	EIAR-CIMMYT	2012	S	poor to good
Kingbird	EIAR-CIMMYT	2014	S-MS	good to very good
Kubsa	EIAR-CIMMYT	1995	S	---
Pavon-76	EIAR-CIMMYT	1982	MS-S	poor to very good
Shorima	EIAR-ICARDA	2011	MS	excellent

(S: susceptible; MS: moderately susceptible).

Experimental design

Two duplicate experiment trials (Figure 1), only differing in their irrigation scheme, were set up based on a modified random complete block design. The six selected wheat varieties were planted at Trial 1 on February 11, 2023, and at Trial 2 on February 13, 2023, in two side-by-side treatment blocks related to disease control, each variety with three randomized replicates, resulting in 36 plots. Each block consisted of three rows 2 m apart from each other, and each row had six plots 1 m apart from each other. Plots had a size of 5 m × 5 m to satisfy the need of a statistically representative sample of spectral satellite information per plot (pixels per plot). Row spacing within each plot was 20 cm. In total, 72 plots were established (2 irrigation schemes × 2 treatment blocks × 6 varieties × 3 replicates).

The two irrigation schemes, based on conventional flooding, differed in their temporal interval. Trial 1 was planned to be flooded on a weekly basis and Trial 2 bi-weekly. However, during almost the entire experiment period, the planned irrigation scheme was affected by rainfall, which is unusual for the off-season. Consequently, both trials were watered equally, except from April 2 to 19, 2023. Only during this 18-days period, irrigation management contrasted as initially planned.

The two blocks at each trial differed in their fungicide treatment to control disease infection. One block was SR-free through fungicide application (herein referred to as "Treated"), and the other block was SR-infected without fungicide control (herein referred to as "Untreated"). Between the two blocks, a strip of 2 m land was left unplanted to avert fungicide drift. Additionally, a plastic sheet was used around each plot as a barrier during fungicide spraying for the treated blocks. Fungicide Nativo SC 300 (trifloxystrobin 100 g/l and tebuconazole 200 g/l; Bayer, Germany) was used at a rate of 0.9 l/ha in 200 l water applied with handheld sprayers on April 7, 2023, and subsequent fungicide applications every 14 days. SR inoculation was conducted through planting a mix of SR-susceptible bread and durum wheat varieties (Ogolcho, Leeds, Malefia, Local Red, and Hidase) as single spreader rows between plots and subsequent application of bulk inoculum of major Pgt races identified in Ethiopia (TTKSK, TKTTF, JRCQC, TTTTF, TTRTF, TTKTT, and TKKTF) from stem elongation (direct plant injection on March 22, 2023; herein referred to as "day after inoculation 0" (DAI 0)) until booting stage (spraying using an Ultra Low Volume atomizer).

Land leveling was carried out before planting, and plots were fertilized with N-P-S at 100 kg/ha and UREA at 50 kg/ha. Entire plots were harvested; grain yield was measured in grams per plot with the grain moisture adjusted to 12% and subsequently converted to tons per hectare (t/ha) [62].

Disease scoring

On DAI 0 (March 22, 2023), baseline disease scoring was carried out. When SR pressure was at ≥1% severity for most untreated plots, scoring was conducted weekly, covering different growth stages from booting (DAI 17; April 08, 2023) to dough (DAI 44; May 5, 2023), five times in total (Figure 2). For each plot, five visual SR sub-scores were taken, one in each corner and one in the center, and subsequently averaged (avg.) into a representative SR score. Additionally, YR and LR scores were taken because natural infection might occur in the research plots. Rust severity was assessed using the Modified Cobb Scale [63], rust incidence and the infection response (pustule type and size) to rust infections according to standardized rust scoring scales [64,65]. Two disease indices (DI), only differing in handling the host infection response information, were calculated per plot: a) DI_{ISHR} by multiplying the rust incidence with the severity intensity and a host response constant, corresponding to a specific host response class [65] using Equation 1 [42]; and DI_{IS} by multiplying the rust incidence with the severity intensity using Equation 2 [26,28–30]. By calculating the DI_{ISHR} and DI_{IS} for each scoring date, disease progression curves were computed.

$$DI_{ISHR} = \frac{F \times D \times HR}{100} \quad \text{(Equation 1)}$$

where DI_{ISHR} is the disease index in percent, F is the incidence value in percent, D is the severity in percent, and HR is the host response constant according to specific host response class [65].

$$DI_{IS} = \frac{F \times D}{100}$$ (Equation 2)

where DI_{IS} is the disease index in percent, F is the incidence value in percent, and D is the severity in percent.

Remote sensing

To analyze satellites' SR disease early detection and severity assessment potential at the plot scale, two state-of-the-art VHRS systems were selected: Pleiades-Neo [34] (Airbus Defence and Space, Toulouse, France) and SkySat [35] (Planet Labs, San Francisco, CA, United States). Their sensors are capable of sub-meter and sub-daily data acquisition, increasing the probability of cloud-free imagery. Such imagery is a prerequisite for in-season crop disease monitoring, especially in regions with high cloud coverage during the cropping season, and small field sizes, commonly found in smallholder cropping systems.

Based on the twin-satellite concept, the Pleiades-Neo constellation includes two identical very high-resolution optical imaging satellites phased at 180° in the same orbit for optimal coverage, high revisit capacity (twice a day), and data delivery. Panchromatic (grayscale) data with the spectral range of 450-800 nm is captured in a single band at the spatial resolution of 0.30 m, and multispectral data in the visible-near-infrared (VNIR) range of the electromagnetic spectrum at 1.2 m spatial resolution. A multispectral dataset has six multispectral broad bands: deep blue (DB; 400-450 nm), blue (B; 450-520 nm), green (G; 530-590 nm), red (R; 620-690 nm), red edge (RE; 700-750 nm), and near-infrared (NIR; 770-880 nm). Two orthorectified, radiometrically corrected, and georeferenced Pleiades-Neo scenes were obtained from Airbus Defence and Space Intelligence (Toulouse, France) through ESA's Third-Party Mission program (Figure 2). Both scenes were delivered as pansharpened (based on Airbus's proprietary fusion model), 6-band ortho products (Full PMS) with 0.3 m spatial resolution, corrected from systematic atmospheric effects to top-of-atmosphere reflectance. The reflectance values can be directly assimilated to ground surface reflectance, if imagery was acquired in clear sky conditions [66]. Pansharpening is a method to increase the spatial resolution of multispectral information by fusing a higher spatial resolution panchromatic image with a lower spatial resolution multispectral image [67,68].

The SkySat constellation consists of 21 high-resolution earth imaging nano-satellites (CubeSats). The constellation is capable of recording panchromatic and multispectral imagery at spatial resolutions of 0.57-0.86 m and 0.75-1.0 m, respectively, up to 6-7 times per day. The panchromatic single-band image covers the spectral range of 450-900 nm. The multispectral image has four multispectral broad bands: B (450-515 nm), G (515-595 nm), R (605-695 nm), and NIR (740-900 nm). Four orthorectified, radiometrically calibrated and georeferenced SkySat scenes were obtained through ESA's Third-Party Mission program, delivered as pansharpened, 4-band multispectral SkySat Ortho Analytic Surface Reflectance products (Figure 2). These scenes had a 0.5 m spatial resolution, corrected to bottom-of-atmosphere reflectance.

All VHRS datasets were manually co-registered to seven ground control points (GCPs) installed at the experimental trials using ArcGIS Desktop 10.8.1 (ESRI Inc., Redlands, CA, United States).

Spectral exploratory analysis

A spectral exploratory analysis was conducted using VHRS broad-band physiological indices. Two generic formulas were applied to VHRS datasets to compute spectral indices based on complete two by two combinations of spectral bands. The ratio spectral index (RSI) and the normalized difference spectral index (NDSI) were calculated based on Equations 3 and 4, respectively.

$$RSI(i,j) = \frac{R_i}{R_j} \quad \text{(Equation 3)}$$

$$NDSI(i,j) = \frac{R_i - R_j}{R_i + R_j} \quad \text{(Equation 4)}$$

where R_i and R_j are the reflectance for satellite wavelength bands *i* and *j*, respectively.

Established VIs such as the Blue Green Pigment Index (BGI), Ratio Index Red/Green (RGR), Ratio Vegetation Index (RVI), and the Simple Ratio (SR) are examples of RSIs based on the simple ratio concept of B/G, R/G, R/NIR, and NIR/R bands, respectively. Green Normalized Difference Vegetation Index (GNDVI), Normalized Difference Vegetation Index (NDVI), Normalized Pigment Chlorophyll Ratio Index (NPCI), Normalized Green Red Difference Index (NGRDI), and Normalized Difference Red Edge Index (NDRE) are well-known representations of NDSIs using NIR-G, NIR-R, R-B, G-R, and NIR-RE bands, respectively [42,51,69]. The concept of complete two by two combinations of spectral bands and derived RSI and NDSI formulas were adapted from previous studies related to hyperspectral RS applications [69–75]. Besides generic physiological indices, ten more complex VIs related to wheat diseases and chlorophyll have been computed from SkySat and Pleiades-Neo imagery (Supplementary Data S1). In total, 37 and 76 spectral features were obtained for SkySat and Pleiades-Neo, respectively.

To prevent mixed pixels from spreader rows and paths, plot polygons were reduced by a 1 m buffer. As the mean per plot, spectral features such as native spectral bands and spectral indices (VIs, RSIs, and NDSIs) were extracted from both Pleiades-Neo and SkySat time series per acquisition date.

Data analysis

VHRS datasets were acquired over both experimental trials, and ground truthing in the form of visual disease scoring was carried out. Cloud-free SkySat imagery could not be acquired on DAI 23 due to weather conditions. Figure 2 shows the data collection timeline across key vegetative and reproductive growth stages from booting to dough.

<table>
<tr><td rowspan="2">Satellite</td><td>Pleiades-Neo</td><td></td><td></td><td></td><td></td><td></td><td></td><td>PN[2]</td><td>PN[1]</td></tr>
<tr><td>SkySat</td><td></td><td></td><td></td><td></td><td>SS[2]</td><td>SS[1]</td><td>SS[2]</td><td>SS[1]</td></tr>
<tr><td>In Situ</td><td>Scoring</td><td></td><td></td><td>SCORE</td><td></td><td>SCORE</td><td>SCORE</td><td>SCORE</td><td>SCORE</td></tr>
<tr><td colspan="2">Management</td><td>$PL_{Site\ 1}$</td><td>$PL_{Site\ 2}$</td><td>IN</td><td>FA</td><td></td><td>FA</td><td></td><td>FA</td></tr>
<tr><td colspan="2">Growth stage (Site 1|2)</td><td></td><td></td><td></td><td></td><td>B-H|B</td><td>Mi|Mi</td><td>D|D</td><td>D|D</td></tr>
<tr><td colspan="2">DAI</td><td></td><td></td><td>0</td><td>16</td><td>17</td><td>30</td><td>37</td><td>44</td></tr>
<tr><td colspan="2">Date</td><td>11-Feb</td><td>13-Feb</td><td>22-Mar</td><td>07-Apr</td><td>08-Apr</td><td>21-Apr</td><td>28-Apr</td><td>05-May</td></tr>
</table>

Figure 2. Overview of the data collection timeline (PN: Pleiades-Neo; SS: SkySat; [1, 2] satellite data acquisition ±1 day and ±2 days apart from scoring date, respectively; int: interpolated; PL: planting; IN: last day of inoculation of SR; FA: fungicide application; B: booting; H: heading; F: flowering; Mi: milking; D: dough; DAI: day after inoculation).

The area under the curve (AUC) was derived for each spectral feature (DAI 17-44) using the trapezoidal method, i.e., Riemann's integrals [76]. From disease scoring data (here: DI_{ISHR}), the area under the disease progress curve (AUDPC) was calculated for the period DAI 17-44 based on Riemann's integrals. Consequently, the above calculations enabled the aggregation of the temporal information from disease scores and VHRS datasets into single variables (AUDPC and AUC). To assess the early detection potential of specific VHRS sensors, a Pearson correlation analysis was carried out, evaluating the relationship between disease scoring (severity, DI_{ISHR}, and DI_{IS}) and spectral features per DAI. The individual relationships between data from AUDPC and AUCs, AUDPC and grain yield, and AUCs and grain yield were investigated using Pearson correlation analysis. The data processing and analyses were performed using statistical software R, version 4.4.1 [77].

Results

Temporal stem rust progression

According to the visual disease scoring, an early natural YR infection occurred, and SR infection was established successfully (Supplementary Data S2-S5), while LR was not observed. Figure 3 shows disease progression curves based on DI_{ISHR} per wheat variety and treatment blocks for YR and SR, respectively. YR and SR were present with varying intensity in the plots on all scoring dates, except on DAI 0. The scoring data confirms the effectiveness of fungicide applications in treated blocks, maintaining disease pressure to very low levels (DI_{ISHR} <0.5%). Only Hidase showed initial SR infection symptoms (DAI 17) that were controlled after first fungicide application. Of all varieties, only Kubsa was heavily affected by YR in the untreated blocks, rapidly increasing from a mild infection on DAI 17 (DI_{ISHR} 1-4%) to a severe infection on DAI 30 (DI_{ISHR} 37-44%). On other varieties, YR impact was minor (DI_{ISHR} ≤1%), except for Hidase on DAI 30 (Trial 1: DI_{ISHR} 5.2%) and Pavon-76 on DAI 37 (Trial 2: DI_{ISHR} 7.7%). To avoid mixed disease effects, Kubsa was removed from further data analysis.

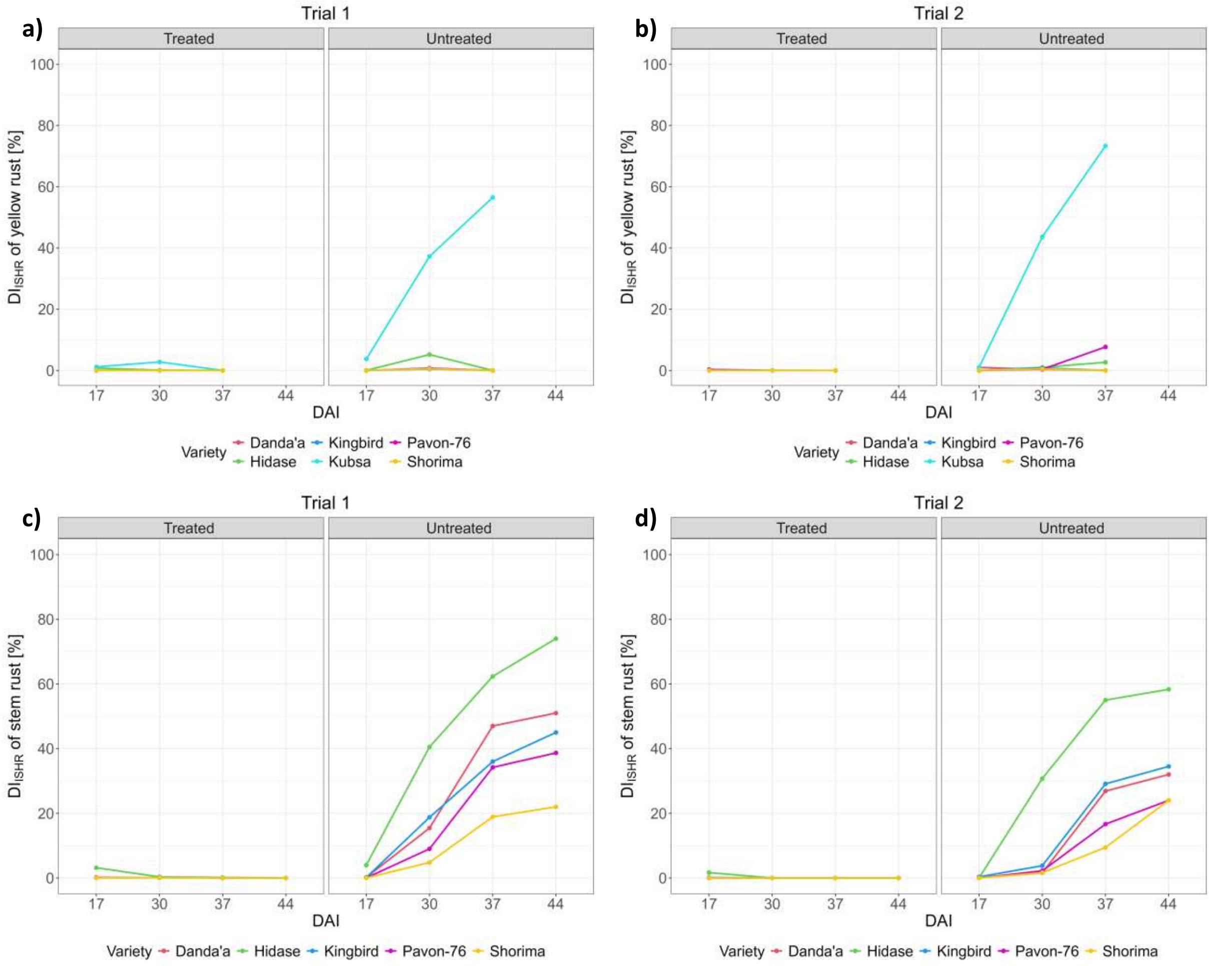

Figure 3. Disease progression (expressed by disease index (DI_{ISHR})) per wheat variety and treatment block for Trials 1 and 2 – YR (**a**, **b**) and SR (**c**, **d**) (note: variety Kubsa was excluded for SR).

Overall, the SR scorings support the expected variety response to SR based on previous reports (Table 1). The most susceptible variety, Hidase (S) exhibited rapid disease development, followed by less susceptible varieties Danda'a and Kingbird (both S-MS) and Pavon-76 (MS-S). The least susceptible variety, Shorima (MS), exhibited the lowest disease development. The untreated blocks in both trials exhibited similar patterns of variety response to SR disease presence. Compared to Trial 2, SR disease pressure developed faster and more intensely across all varieties at Trial 1; i.e., clearly observed on DAI 30 and DAI 37. Due to the 18-days difference in the irrigation scheme (April 2-19, 2023), the weekly irrigation increased the environmental conduciveness for SR development at Trial 1, as reflected in the SR scoring data (DAI 17-30). Starting from DAI 44, a 100% SR incidence rate was recorded for all varieties in the untreated blocks at both trials, showing host plant reactions between MS and S, except for one plot of Shorima at Trial 1 (MR-MS). SR severity rates varied between 30% (Shorima) and 80% (Hidase) at Trial 1 and 20% (Pavon-76) and 70% (Hidase) at Trial 2. SR severity rates between 50-80% and at least moderately susceptible to fully susceptible host response (MS-S) of most untreated varieties meant that plants were largely dead by this time, observed for most uncontrolled plots at Trial 1. In contrast, uncontrolled plots at Trial 2 varied between moderately and severely diseased (20% MS to 40% MS-S) and only Hidase (50% MS-S and 60-70% S) can be considered having dead plants.

Based on our observations, the vigor of varieties in terms of crop health and vitality in untreated blocks can be conservatively categorized into disease scenarios for each DAI according to the SR impact, expressed as DI_{ISHR}, averaged across all varieties per untreated block and DAI: healthy (avg. DI_{ISHR} <1%), mildly diseased (avg. DI_{ISHR} 1-14.9%), moderately diseased (avg. DI_{ISHR} 15-29.9%), severely diseased (avg. DI_{ISHR} 30-44.9%), and fully diseased (avg. DI_{ISHR} ≥45%) (Table 2).

Table 2. Disease scenarios per DAI – SR-related DI_{ISHR} (%) for each variety and averaged across all varieties per untreated block for each trial and corresponding vigor category.

Trial 1

Variety/DAI	**17**	**30**	**37**	**44**
Danda'a	0.2	15.5	47.0	51.0
Hidase	4.0	40.5	62.3	74.0
Kingbird	0.2	18.8	36.0	45.0
Pavon-76	0.0	9.0	34.2	38.7
Shorima	0.0	4.8	18.9	22.0
Mean	0.9	17.7	39.7	46.1
Scenario	healthy	moderately diseased	severely diseased	fully diseased

Trial 2

Variety/DAI	**17**	**30**	**37**	**44**
Danda'a	0.0	1.6	26.9	32.0
Hidase	0.0	30.7	55.0	58.3
Kingbird	0.4	3.8	29.1	34.5
Pavon-76	0.0	2.2	16.7	24.0
Shorima	0.0	1.6	9.5	24.0
Mean	0.1	8.0	27.4	34.6
Scenario	healthy	mildly diseased	moderately diseased	severely diseased

green: healthy (avg. DI_{ISHR} <1%); yellow: mildly diseased (avg. DI_{ISHR} 1-14.9%); orange: moderately diseased (avg. DI_{ISHR} 15-29.9%); red: severely diseased (avg. DI_{ISHR} 30-44.9%); and grey: fully damaged (avg. DI_{ISHR} ≥45%).

Stem rust impact on yield

Results of yield performance of individual varieties under both fungicide treatments are shown in Table 3. Yield production differed significantly ($P < 0.001$) between the treated and untreated blocks at both trials. In the treated blocks at Trial 1 and Trial2, the average yield across all varieties was 4.4 t/ha and 4.3 t/ha, respectively, while in the untreated blocks reached 1.0 t/ha and 1.3 t/ha, respectively. Overall, relatively low variations were observed for plot yields per variety in treated blocks (variance: <0.15 t/ha) and untreated blocks (variance: <0.25 t/ha) at both trials. In the untreated blocks, minimum yield was recorded for more susceptible varieties Hidase (both trials: 0.4 t/ha) and Danda'a (Trial 1: 0.5 t/ha; Trial 2: 0.7 t/ha) and maximum yield for less susceptible varieties Shorima (Trial 1: 1.7 t/ha; Trial 2: 1.9 t/ha) and Pavon-76 (Trial 1: 1.2 t/ha; Trial 2: 1.9 t/ha) (Figure 4). Across all varieties, yield was decreased by SR within the untreated plots at both trials. Yield loss can be associated with the degree of varieties' SR susceptibility, i.e., highest yield loss in the most susceptible varieties (Hidase: 91-93%; Danda'a: 84-90%) and lowest yield loss in the least susceptible variety (Shorima: 48-56%). For untreated plots at both trials, the correlation analysis revealed a strong ($|r|$: 0.6-0.79) negative and significant relationship between yield and AUDPC (Trial 1: $r = -0.76$; Trial 2: $r = -0.75$; $P < 0.01$) (Figure 5). Plot-level variations in terms of yield and disease pressure (AUDPC) can be observed for single varieties. All untreated varieties showed very low plot-level variations in yield (variance: ≤0.07 t/ha), except Shorima (both trials) and at Trial 2 Pavon-76 and Kingbird (variance: 0.18-0.23 t/ha), while plot-level variations in AUDPC clearly differed between trials, especially with higher variations for Danda'a and Pavon-76 at Trial 2 (Figure 4). Results clearly show the anticipated variety reaction to SR, already considered when selecting the varieties.

Table 3. Average grain yield (t/ha) and yield loss (%) per variety caused by SR calculated as the percentage difference in grain yield (t/ha) between fungicide and non-fungicide treatments.

Variety	Trial 1					Trial 2				
	TREATED		UNTREATED		Yield Loss	TREATED		UNTREATED		Yield Loss
	Yield	AUDPC	Yield	AUDPC		Yield	AUDPC	Yield	AUDPC	
Danda'a	4.9	1.9	0.5	663.2	90	4.5	0.0	0.7	315.9	84
Hidase	4.8	25.4	0.4	1126.3	93	4.9	10.9	0.4	896.7	91
Kingbird	4.0	1.2	1.4	598.1	66	4.3	0.9	1.7	364.6	59
Pavon-76	4.6	1.1	1.2	465.0	73	4.4	0.0	1.9	222.7	56
Shorima	3.9	1.2	1.7	257.4	56	3.6	0.0	1.9	166.5	48
Mean	4.4	6.2	1.0	622.0	76	4.3	2.4	1.3	393.3	68

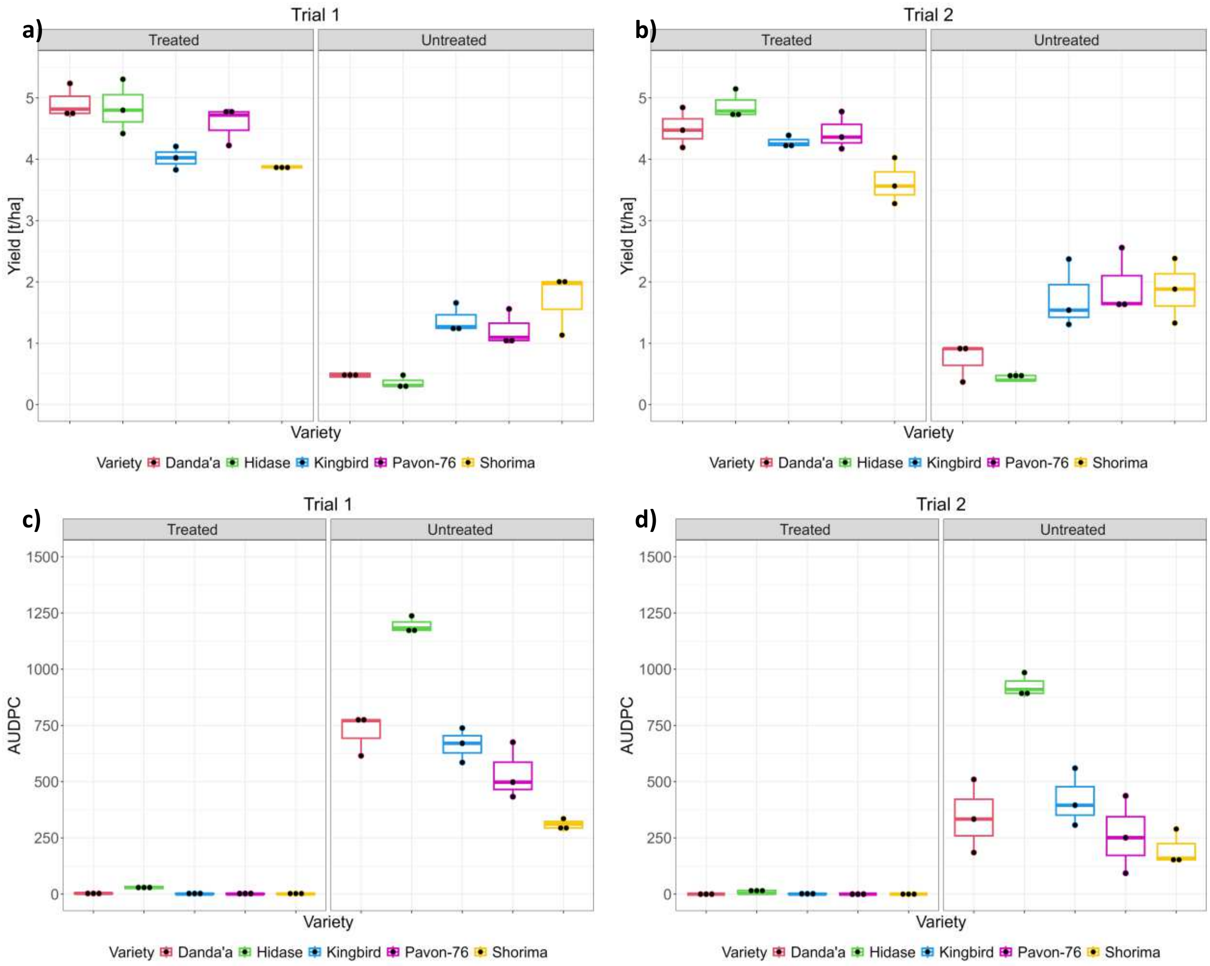

Figure 4. Box plot per wheat variety and treatment block of Trials 1 and 2, showing variations of recorded yield (**a**, **b**) and AUDPC (**c**, **d**).

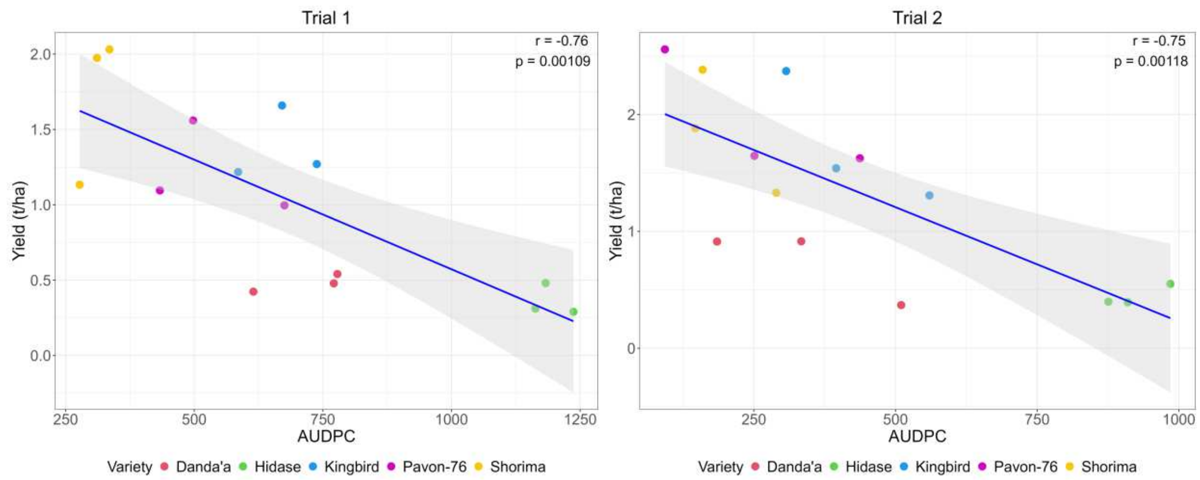

Figure 5. Correlation between grain yield and AUDPC for untreated blocks of Trials 1 and 2.

Satellite time series and multispectral profiles

For each untreated block, the time series from SkySat (Figure 6) and Pleiades-Neo (Supplementary Data S6) reveal in detail the temporal alteration of wheat canopies affected by SR pressure and variety's susceptibility in each plot. Overall, the sequence of SR impact on wheat canopies as seen in the time series is aligned to the results of the SR scoring. The imagery confirms that the canopy changes at both trials do not occur synchronously in terms of speed and damage impact. At Trial 1, a drastic change from DAI 37 to DAI 44 can be clearly observed in the untreated block, shifting from a relatively still green, but strongly diseased, wheat canopy (DAI 37) to a totally diseased wheat canopy with dead plant tissue and fully developed necrosis across almost all plots (DAI 44). As this shift significantly alters the spectral response, the creation of the additional disease scenario (fully diseased) is clearly needed for SR monitoring.

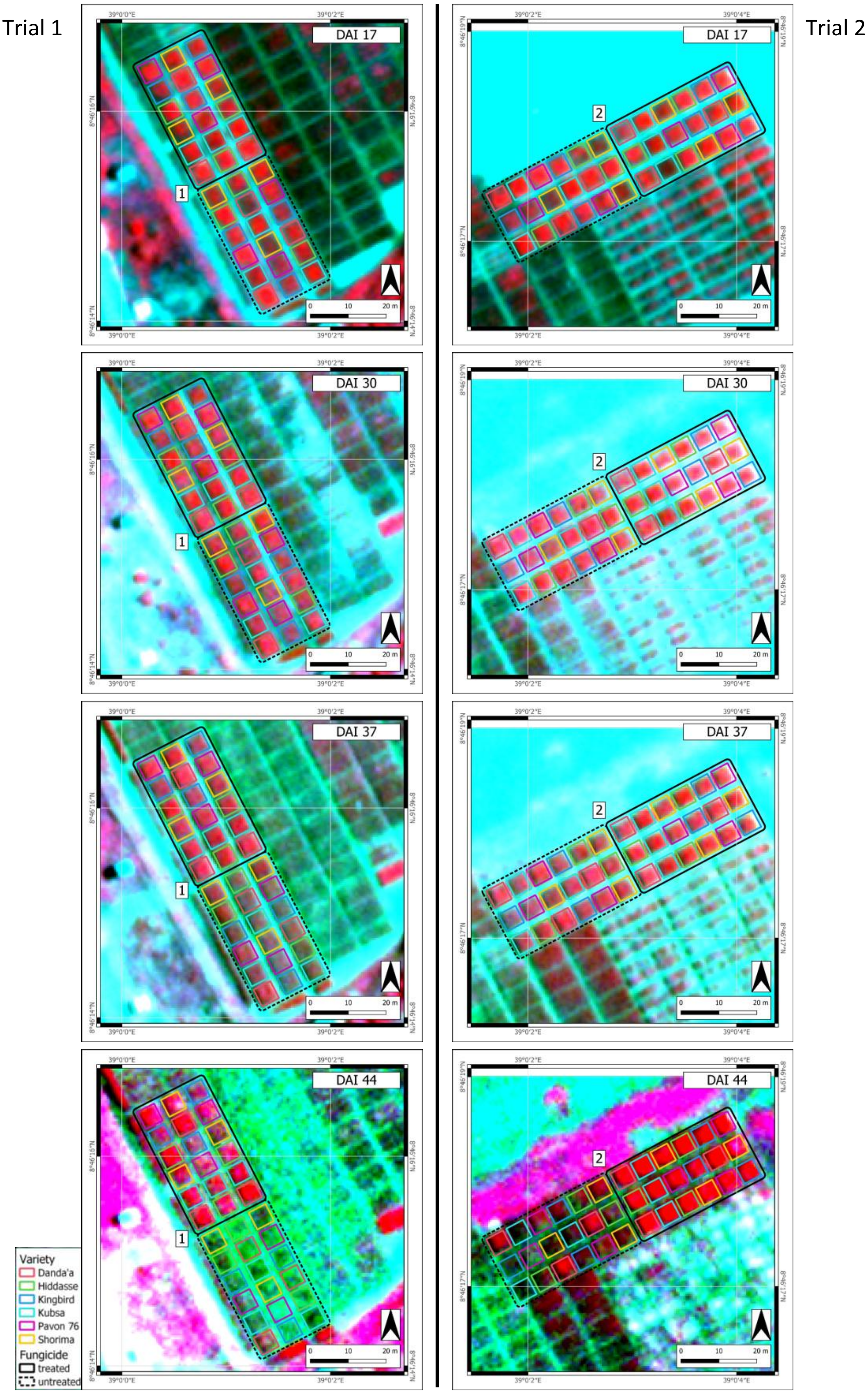

Figure 6. The spectral signal derived from SkySat time series reveals wheat canopy changes (SkySat false color composites using near-infrared, red, and green bands from corresponding DAIs). Figures prepared using QGIS version 3.28.11-Firenze [57].

Early detection and monitoring of stem rust

In each untreated block, the relationship between visual SR scores and spectral features from both VHRS sensors, were statistically assessed across all different varieties at the plot level for each DAI (DAI 17-44), separately. This temporal period covers all disease scenarios from healthy to fully diseased (Table 2). Using Pearson correlation analysis, Figures 7 and 8 summarize significant relationships of SkySat and Pleiades-Neo spectral features with disease metrics such as severity, DI_{ISHR}, and DI_{IS} at each DAI for untreated blocks of both trials, respectively (complete results are presented in Supplementary Data S7-S12).

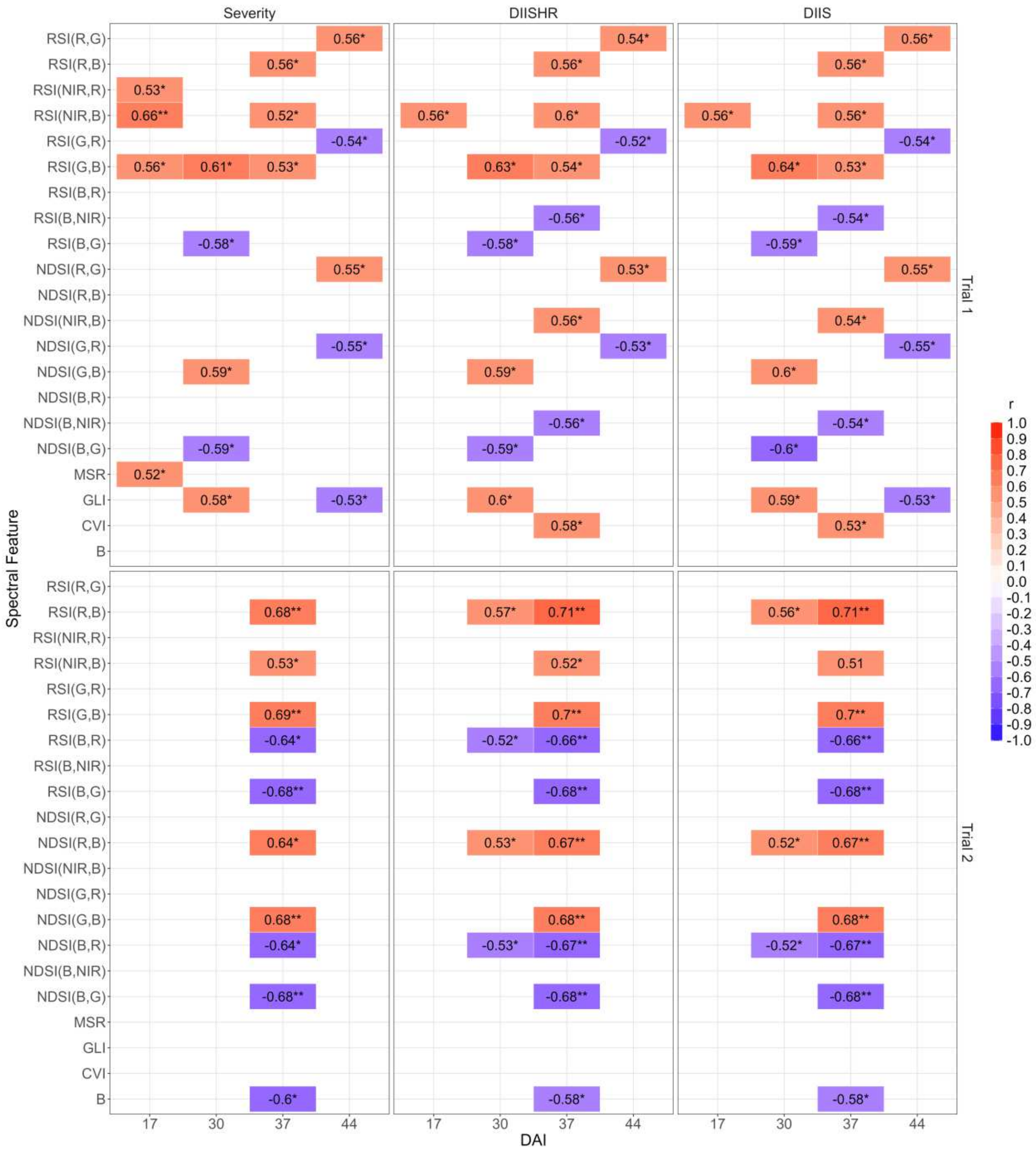

Figure 7. Significant correlations (Pearson) between disease metrics and SkySat spectral features at each DAI (both trials, untreated blocks) (P = p-value; **P* < 0.05; ***P* < 0.01).

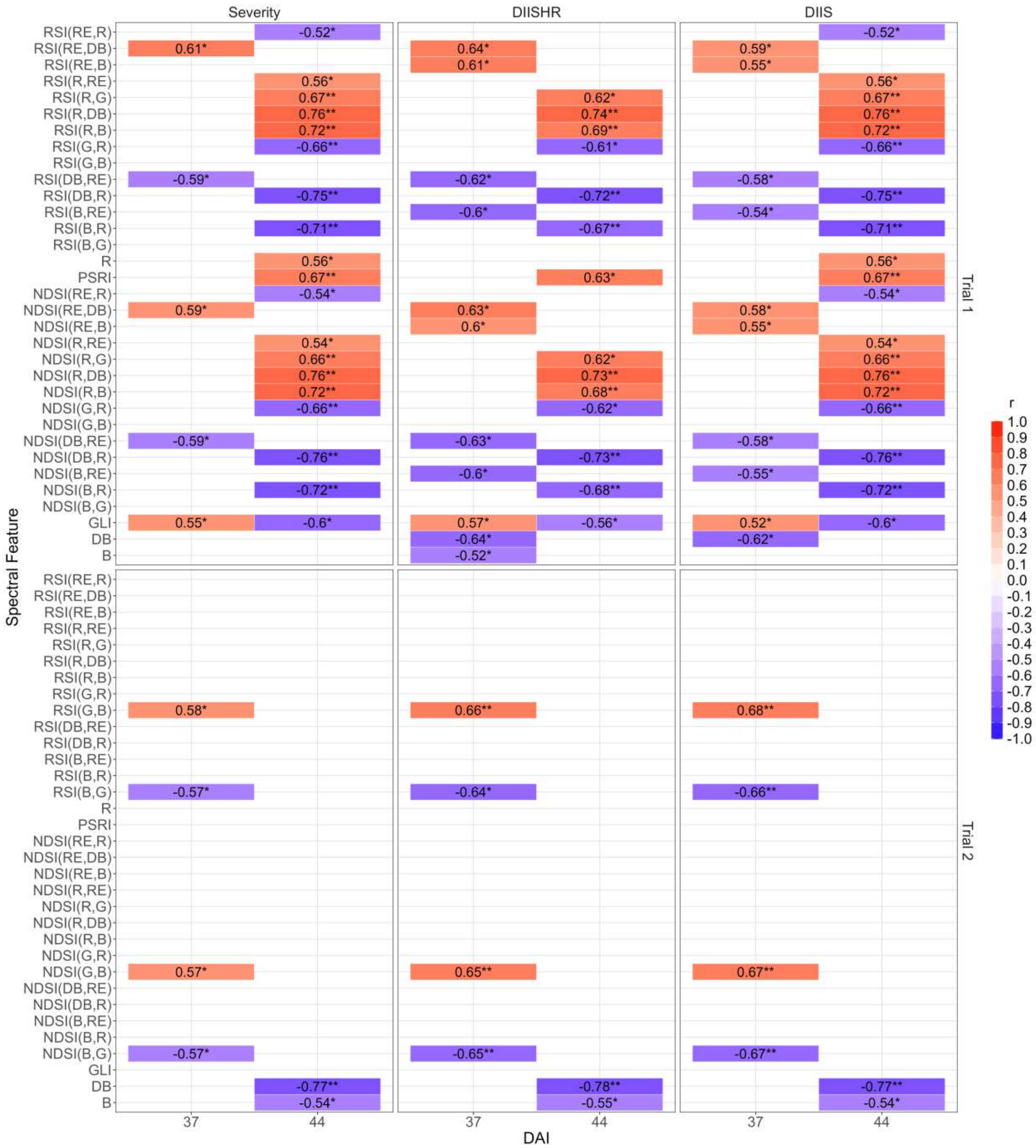

Figure 8. Significant correlations (Pearson) between disease metrics and Pleiades-Neo spectral features at each DAI (both trials, untreated block) (P = p-value; **P* < 0.05; ***P* < 0.01; ****P* < 0.001).

For both VHRS sensors, significant (*P* < 0.05) positive and negative moderate (|r|: 0.4-0.59) to strong (|r|: 0.6-0.79) correlations with all disease metrics were found for multiple spectral features across all DAIs at both trials, except at Trial 2 on DAI 17 due to no disease pressure (DI_{ISHR} 0.1%; Table 2) and on DAI 44 only for SkySat most likely due to sensor's limited spectral resolution. In contrast at Trial 2 on DAI 44, Pleiades-Neo was found highly significant (*P* < 0.001) in the DB spectral band, a spectral region not covered by SkySat. Also, at Trial 2 on DAI 30, correlations were not found with severity.

The observed significant spectral features were largely identical across all disease metrics. The highest, significant correlations were obtained for SkySat and Pleiades-Neo with RSIs, slightly stronger than NDSIs, having a positive direction, except for Pleiades Neo at Trial 1 on DAI 37 (DI_{IS}) and Trial 2 on DAI

44 (all metrics). This suggests that the higher the spectral reflectance is, the higher the SR pressure and damage in the corresponding variety.

At both trials, the Pearson coefficient revealed for SkySat that the visible B band in diverse RSI and NDSI combinations with G, R, or NIR bands played the most important role for SR detection across all disease metrics and from healthy to severely diseased scenarios, while for Pleiades-Neo, DB and B bands were key in RSI and NDSI combinations with RE or G, but also as native bands. Once varieties were mostly fully diseased (Trial 1; DAI 44), moderate (SkySat) and strong (Pleiades-Neo) Pearson coefficients indicated a shift from DB or B band-based RSIs and NDSIs towards RSIs and NDSI with R-G band combinations for both sensors and only for Pleiades-Neo RSIs and NDSIs with R-DB or R-B band combinations. Table 4 displays the most relevant VHRS spectral features for each disease scenario.

Table 4. Most relevant VHRS spectral features for each scenario based on averaged Pearson correlation ($|r_{mean}|$) across disease metrics.

Scenario	SkySat			Pleiades-Neo		
	Spectral feature	***n***	**$|r_{mean}|$**	**Spectral feature**	***n***	**$|r_{mean}|$**
Healthy	RSI(NIR,B)	3	0.59			
Mildly	RSI(R,B)	2	0.57			
	NDSI(B,R)	2	0.53			
	NDSI(R,B)	2	0.53			
Moderately	RSI(G,B)	6	0.66	RSI(G,B)	3	0.64
	NDSI(B,G)	6	0.64	NDSI(B,G)	3	0.63
	NDSI(G,B)	6	0.64	NDSI(G,B)	3	0.63
	RSI(B,G),	6	0.63	RSI(B,G)	3	0.62
Severely	RSI(R,B)	3	0.56	DB	5	0.72
	RSI(NIR,B)	3	0.56	RSI(RE,DB)	3	0.61
	RSI(G,B)	3	0.53	NDSI(RE,DB)	3	0.60
				NDSI(DB,RE)	3	0.60
				RSI(DB,RE)	3	0.60
Fully	RSI(R,G)	3	0.55	RSI(R,DB)	3	0.75
	NDSI(G,R)	3	0.54	NDSI(R,DB)	3	0.75
	NDSI(R,G)	3	0.54	NDSI(DB,R)	3	0.75
	RSI(G,R)	3	0.53	RSI(DB,R)	3	0.74
				RSI(R,B)	3	0.71
				NDSI(B,R)	3	0.71
				NDSI(R,B)	3	0.71
				RSI(B,R)	3	0.70
				PSRI	3	0.66
				RSI(R,G)	3	0.65
				NDSI(R,G)	3	0.65
				NDSI(G,R)	3	0.65
				RSI(G,R)	3	0.64
				GLI	3	0.59

For SkySat and across all disease metrics, the earliest significant correlation was observed with RSI(NIR,B) (healthy scenario), when Hidase was the only variety affected by SR (DI_{ISHR} 4%). For the mildly diseased scenario, RSIs and NDSIs with B-R band combinations were also moderately significantly correlated, mostly driven by the already severely diseased Hidase (Table 2), while other varieties remained mildly diseased (DI_{ISHR} 1.6-3.8%). For the moderately diseased scenarios, the strongest correlations were identified using RSIs and NDSIs with B-G band combinations. Only at Trial 1, moderate to strong relationships were found with RSIs and NDSIs with B and G, R, or NIR band combinations for the severely diseased scenario. These results indicate the potential of early detection, in terms of low disease infection levels, and monitoring SR from mild to severe infection stages using SkySat imagery. For the fully diseased scenario, the strongest correlation was found with RSI(R,G) Key SkySat spectral features such as RSI(NIR,B), RSI(R,B), RSI(G,B), but also NDSI(B,R) and NDSI(R,B) revealed significant relationships for multiple scenarios, i.e., RSI(NIR,B) for healthy, moderately, and severely scenarios (all metrics), RSI(R,B) for mildly, moderately, and severely scenarios (DI_{ISHR} and DI_{IS}), and RSI(G,B) for healthy, moderately, and severely scenarios (only severity) (Figure 7, Table 4).

Using Pleiades-Neo confirms the findings with SkySat for the moderately diseased scenarios. For the severely diseased scenario, Pleiades-Neo features revealed strong correlations for the native DB band and for RSI and NDSIs with DB-RE or B-RE band combinations and moderate correlations for the native B band. For the fully diseased scenario, Pleiades-Neo showed strong correlations using RSIs and NDSIs with R-G band combinations (like SkySat), surpassed by R-B and R-DB combinations (Figure 8, Table 4). Several chlorophyll-sensitive VIs were the only more complex VIs that significantly ($P < 0.05$) correlated with the disease scoring: SkySat-derived CVI and GLI for severely and moderately diseased scenarios, respectively, and Pleiades-Neo-derived GLI for severely and fully diseased scenarios and PSRI for the fully diseased scenario.

VHRS high-throughput phenotyping

Focusing on the untreated blocks, the relationships of the AUCs of SkySat spectral features, such as individual bands, VIs, RSIs, and NDSIs, with the AUDPC and yield were statistically evaluated at the plot level (Supplementary Data S13). Table 5 summarizes the significant relationships with AUDPC for untreated blocks at Trial 1 and Trial 2.

Table 5. Significant correlations (Pearson) of the AUCs of SkySat spectral features with AUDPC (untreated block) (*P* = p-value; **P* < 0.05; ***P* < 0.01).

Trial 1			**Trial 2**		
AUC of spectral feature	**r**	***P***	**AUC of spectral feature**	**r**	***P***
NDSI(B,G)-AUC	-0.6*	0.018	NDSI(B,R)-AUC	-0.7**	0.003
NDSI(G,B)-AUC	0.6*	0.018	NDSI(R,B)-AUC	0.7**	0.003
RSI(B,G)-AUC	-0.57*	0.025	NDSI(B,G)-AUC	-0.67**	0.006
RSI(NIR,B)-AUC	0.57*	0.026	NDSI(G,B)-AUC	0.67**	0.006
B-AUC	-0.55*	0.034	RSI(B,R)-AUC	-0.64**	0.009
RSI(G,B)-AUC	0.54*	0.039	RSI(B,G)-AUC	-0.63*	0.012
NDSI(B,R)-AUC	-0.52*	0.045	B-AUC	-0.54*	0.039
NDSI(R,B)-AUC	0.52*	0.045			

For AUDPC, Pearson correlation analysis revealed that only AUCs of B band-based spectral features have significant ($P < 0.05$) positive and negative moderate to strong correlations. Observed significant B band-based RSI and NDSI combinations with G or R bands as well as native B bands were found to be consistently sensitive across trials, except RSI(B,R) and RSI(G,B). At Trial 1, the strongest correlations were achieved using NDSI(B,G)-AUC and NDSI(G,B)-AUC (both: $|r| = 0.6$) and at Trial 2 using NDSI(B,R)-AUC and NDSI(R,B)-AUC (both: $|r| = 0.7$). The data suggest that the varieties with higher B-AUCs and AUCs of RSIs and NDSIs that uses the spectral information of the B band as first input variable in its calculation (e.g., RSI(B,G)) also had lower disease pressure in terms of AUDPC (negative correlation). While varieties with higher AUCs of RSIs and NDSIs that use the spectral information of the B band as second input variable in its calculation (e.g., RSI(G,B)) had higher disease pressure in terms of AUDPC (positive correlation). For yield, significant (P < 0.05) relationships could not be observed at any trial (Supplementary Data S13).

Discussion

To the best of our knowledge, this is the first study to investigate satellite capabilities for detecting, monitoring, and phenotyping SR in wheat at the plot level across healthy, mild, moderate, severe, and fully diseased situations, covering vegetative and reproductive growth stages. Previous satellite-based research for wheat diseases has primarily focused on foliar pathogens such as YR and targeted grain filling as the optimal time for mono-temporal mapping [27,28,30,31,43–47], while early-stage detection remains comparatively unexplored [29,33,42,50]. Early monitoring is particularly valuable, as SR damage increases with earlier infections [42]. Here, we focused on the booting, heading, and flowering stages preceding grain filling.

Because SR development depends more on host susceptibility and environmental conditions than phenology, the two trials showed different temporal SR dynamics, driven largely by short-term changes in moisture availability. To obtain comparable disease development situations reflecting whole-canopy SR impact under varying host susceptibility and moisture, disease scenarios were defined using average DI_{ISHR} thresholds across varieties, mirroring the approach in [54] while extending it to include a “fully diseased” scenario. These categories provided consistent descriptions of canopy-level SR impact from healthy through fully damaged conditions. Using averaged DI_{ISHR} thresholds across varieties to define disease scenarios also helped ensure that the spectral responses reflected SR progression rather than inherent varietal differences.

Both trials showed similar varietal disease progression patterns. For example, the highly susceptible variety Hidase showed DI_{ISHR} increases of 55-58% within 20 days (DAI 17-37), consistent with reported SR development rates (e.g., ≤80% within 2-3 weeks) [12,42]. Faster disease development under higher moisture in Trial 1 confirms increased humidity as a key environmental driver for SR development on wheat [65,78,79].

Yield losses reached 48-56% in moderately susceptible and up to 93% in susceptible varieties under very strong SR pressure, aligning with reports of up to 100% loss [80]. Across all SR infection response levels, a higher yield loss was observed for all varieties under increased moisture conditions, which is relevant given the expansion of irrigated wheat areas [81]. Significant correlations between AUDPC and grain yield reinforce the high yield-loss risk, consistent with historical SR epidemics such as the severe epidemic in Ethiopia on the susceptible variety Digelu [14].

Multispectral and hyperspectral sensing technologies have been widely used in disease detection and phenotyping [25,36,52,53,82–86]. A recent review on RS for wheat rusts [52] reported accuracies for YR and LR using multispectral satellites (57-90%), low-altitude systems (60-91%), and field spectrometers (71-97%), while SR-specific studies were lacking. UAV-based hyperspectral SR detection reached ≤85% accuracy [54], with sensitive wavelengths in R, RE, and NIR regions for mild and severe classes and in B and NIR regions for moderate classes.

Across early disease stages (healthy, mild, moderate; DI_{ISHR} <30%), SR sensitivity was driven exclusively by SkySat B-based RSIs and NDSIs, found consistent across disease metrics. For healthy canopies, RSI(NIR,B) was most sensitive; R-B features dominated for mild infections; and G-B features were strongest for moderate infections on both sensors. This moderate scenario represented a favorable detection window, ~7 days before severe symptoms are expected. However, this peak reflects a dataset-specific contrast window where epidermal surface perturbations (via B) and emerging pigment changes (via G) overlapped. SR remained detectable at lower severities. In late disease stages (severe, fully diseased; DI_{ISHR} ≥30%), spectral sensitivity shifted toward R- and RE-driven behavior. The severe stage showed less consistency in terms of spectral features across trials and sensors, likely due to genotype-by-environment interactions. For Pleiades-Neo, the most sensitive features included DB and RE-DB, while SkySat showed strongest responses in R-B, NIR-B, and G-B. Once fully diseased, spectral sensitivity shifted toward R-G-based features for both sensors and toward R-DB and R-B for Pleiades-Neo. These patterns align with advanced pigment loss, necrosis, and structural decline. Several SkySat indices were consistently informative across stages, including RSI(NIR,B) (healthy, moderate, severe), RSI(R,B) (mild to severe), and RSI(G,B) (healthy, moderate, severe). Beyond canopy damage assessment, these results show that VHRS imagery captures SR from early infection levels, before visible damage becomes pronounced, consistent with UAV hyperspectral work [54] and studies on other foliar diseases [27,30,43,45,47,87].

SkySat features (e.g., B-G, B-R) correlated moderately to strongly with AUDPC under non-fungicide conditions, underscoring their utility for SR phenotyping. Limited spectral-yield correlations are expected due to the decoupling between canopy-level physiological stress signals and final yield, as SR-induced yield loss is driven by damage mechanisms (e.g., assimilate diversion, infection timing, and source-sink disruption), which are not directly captured by canopy reflectance [24,51]. Inherent varietal yield potential and the fact that our satellite acquisitions ended at the dough stage – before the main grain-filling and yield-formation period – likely further weakened spectral-yield correlations.

SR alters wheat canopy reflectance through pigment, structural, and physiological changes that manifest as chlorosis, necrosis, and formation of uredinia and later telia. As SR progresses, chlorophyll degradation increases reflectance in chlorophyll absorption regions (B: 400-475 nm and R: 620-690 nm), while healthy canopies maintain low reflectance and peak in the G region (520-580 nm), consistent with pigment-reflectance relationships [88,89]. Early-stage SR infection affects B-region reflectance before visible symptoms develop [54,90]. Fungal penetration disrupts the cuticle and upper epidermis, altering surface scattering and pigment absorption dynamics [3,4,91]. Because B wavelengths have shallow penetration depths and are highly sensitive to surface-layer scattering, even subtle early perturbations in cuticular waxes and epidermal pigments measurably affect their reflectance before major mesophyll-level chlorophyll loss occurs [91,92]. Our findings reflect this mechanism: during early-stage infection, the most sensitive features were B-based two-band indices (healthy: NIR-B; mild: R-B; moderate: G-B), capturing the interplay between early epidermal disruption (via B) and emerging pigment changes deeper in the leaf tissue (via G or R). As SR progresses into severe infection, initially small uredinia expand and develop into larger black telial structures, producing pigmented spore masses that absorb visible light, especially in the B and R wavelengths. Concurrently, mesophyll collapse and chlorophyll loss shift the RE (700-750 nm) toward shorter wavelengths – patterns widely reported across wheat rust and other foliar diseases [25,53,93,94]. This matches our finding that severe-stage sensitivity increased for B-based features paired with R, G, or NIR on SkySat (R-B, NIR-B, G-B), and for DB and RE-DB features on Pleiades-Neo, reflecting pigment loss (via R or G), spore pigmentation (via B or DB), and early structural degradation (via RE or NIR). In fully diseased canopies, reflectance was dominated by R-G, R-DB, R-B, and R-RE features, consistent with pigment loss (via R or G), dark spore pigmentation (via B or DB), necrosis (via R), and structural degradation (via RE). Together, these physiological and optical processes explain the early dominance of B-based spectral features, the continued contribution of B and DB under severe infection, with DB effects persisting via R-DB features once fully diseased, and the late-stage dominance of R- and RE-based features. The spectral band configurations of SkySat and Pleiades-Neo align with these mechanistic regions, explaining the observed stage-dependent sensitivity patterns.

While our results demonstrate clear potential for SR detection, distinguishing SR from other biotic and abiotic stresses remains challenging with multispectral data alone. Future work integrating hyperspectral sensing and upcoming satellite missions with enhanced spectral resolution will be essential for improving stress discrimination in farmer fields under realistic conditions.

Our results demonstrate that multispectral VHRS imagery can support high-throughput SR phenotyping and early-stage disease detection at the plot scale. With large imaging footprints, uniform sensors, and standardized processing pipelines, VHRS platforms offer a practical path to scale plot-level assessments toward field- and regional-scale SR monitoring [42,95]. Future work should include additional seasons and locations to strengthen robustness across environments and evaluate the consistency of SR-related spectral responses under varying climatic, management, and disease-pressure conditions.

Conclusions

For wheat breeding and disease surveillance, the capability of multispectral VHRS imagery as a HTP and early SR disease detection tool was assessed at the plot level, focusing on vegetative and reproductive growth stages. A spectral exploratory analysis identified several spectral features from SkySat and Pleiades-Neo satellites that have moderate to strong correlation with SR disease scorings across healthy, mild, moderate, severe, and fully diseased situations. Multispectral broad bands located in the DB to B region of the electromagnetic spectrum played a crucial role for SR detection and monitoring from mild to severe infection levels, with sensitivity shifting toward R-G, R-B, and R-DB features once canopies were fully diseased. Strong correlations fot RSI/NDSI B-G features (|r|: 0.62-0.66), consistent across disease metrics, trials, and sensors, suggest the moderately diseased scenario as a favorable window for early SR detection and timely control measures. SkySat RSI(NIR,B), RSI(R,B), and RSI(G,B) were sensitive across multiple scenarios and reflected reductions in canopy chlorophyll during chlorotic stages. However, similar spectral responses may also arise from other abiotic and biotic stresses. This study provides valuable insights into the potential of multispectral VHRS sensors for SR early detection, monitoring and phenotyping at the plot scale, representing an important step toward upscaling SR surveillance from field trials to regional applications. Future work will expand this framework by incorporating additional seasons and locations, applying machine- and deep-learning approaches, and evaluating SR detection under mixed rust infections and varying management conditions, ultimately supporting robust monitoring systems under realistic field and farm-landscape settings.

References

1. Savary, S. & Willocquet, L. Modeling the Impact of Crop Diseases on Global Food Security. *Annu. Rev. Phytopathol.* **58**, 313–341 (2020).

2. Lidwell-Durnin, J. & Lapthorn, A. The threat to global food security from wheat rust: ethical and historical issues in fighting crop diseases and preserving genetic diversity. *Glob. Food Sec.* **26**, 100446 (2020).

3. Singh, R. P., Huerta-Espino, J. & Roelfs, A. P. The wheat rusts. *FAO Plant Production and Protection Series (FAO)* https://www.fao.org/4/y4011e/y4011e0g.htm (2002).

4. Figueroa, M., Hammond-Kosack, K. E. & Solomon, P. S. A review of wheat diseases—a field perspective. *Mol. Plant Pathol.* **19**, 1523–1536 (2018).

5. Meyer, M. *et al.* Quantifying airborne dispersal routes of pathogens over continents to safeguard global wheat supply. *Nat. Plants* **3**, 780–786 (2017).

6. Bradshaw, C. D. *et al.* Irrigation can create new green bridges that promote rapid intercontinental spread of the wheat stem rust pathogen. *Environmental Research Letters* **17**, 114025 (2022).

7. Hovmøller, M. S., Thach, T. & Justesen, A. F. Global dispersal and diversity of rust fungi in the context of plant health. *Curr. Opin. Microbiol.* **71**, 102243 (2023).

8. Huerta-Espino, J. *et al.* Adult Plant Slow Rusting Genes Confer High Levels of Resistance to Rusts in Bread Wheat Cultivars From Mexico. *Front. Plant Sci.* **11**, 824 (2020).

9. Ristaino, J. B. *et al.* The persistent threat of emerging plant disease pandemics to global food security. *Proceedings of the National Academy of Sciences* **118**, (2021).

10. Singh, B. K. *et al.* Climate change impacts on plant pathogens, food security and paths forward. *Nature Reviews Microbiology 2023 21:10* **21**, 640–656 (2023).

11. Pequeno, D. N. L. *et al.* Production vulnerability to wheat blast disease under climate change. *Nature Climate Change 2024 14:2* **14**, 178–183 (2024).

12. Nazareno, N. R. X. & Roelfs, A. P. Adult Plant Resistance of Thatcher Wheat to Stem Rust. *Phytopathology* **71**, 181–185 (1981).

13. Olivera, P. D. *et al.* Puccinia graminis f. sp. tritici Population Causing Recent Wheat Stem Rust Epidemics in Kazakhstan Is Highly Diverse and Includes Novel Virulence Pathotypes. *Phytopathology* **112**, 2403–2415 (2022).

14. Olivera, P. *et al.* Phenotypic and genotypic characterization of race TKTTF of Puccinia graminis f. sp. tritici that caused a wheat stem rust epidemic in southern Ethiopia in 2013-14. *Phytopathology* **105**, 917–928 (2015).

15. Lewis, C. M. *et al.* Resurgence of wheat stem rust infections in western Europe: causes and how to curtail them. *New Phytologist* **243**, 537–542 (2024).

16. Olivera Firpo, P. D. *et al.* Characterization of Puccinia graminis f. sp. tritici isolates derived from an unusual wheat stem rust outbreak in Germany in 2013. *Plant Pathol.* **66**, 1258–1266 (2017).

17. Saunders, D. G. O., Pretorius, Z. A. & Hovmøller, M. S. Tackling the re-emergence of wheat stem rust in Western Europe. *Communications Biology 2019 2:1* **2**, 1–3 (2019).

18. Patpour, M. *et al.* Wheat Stem Rust Back in Europe: Diversity, Prevalence and Impact on Host Resistance. *Front. Plant Sci.* **13**, 882440 (2022).

19. Patpour, M. *et al.* First Report of Ug99 Wheat Stem Rust Caused by Puccinia graminis f. sp. tritici in South Asia. *Plant Dis.* **108**, 2570 (2024).

20. Meyer, M. *et al.* Wheat rust epidemics damage Ethiopian wheat production: A decade of field disease surveillance reveals national-scale trends in past outbreaks. *PLoS One* **16**, e0245697 (2021).

21. Mekonnen, M. A. *et al.* Unveiling wheat rust epidemics: A long-term surveillance study in Ethiopia’s North Western Amhara region. *Journal of Phytopathology* **172**, e13360 (2024).

22. Meyer, M., Burgin, L., Hort, M. C., Hodson, D. P. & Gilligan, C. A. Large-Scale Atmospheric Dispersal Simulations Identify Likely Airborne Incursion Routes of Wheat Stem Rust Into Ethiopia. *Phytopathology* **107**, 1175–1186 (2017).

23. Kolmer, J. A. Tracking wheat rust on a continental scale. *Curr. Opin. Plant Biol.* **8**, 441–449 (2005).

24. Willocquet, L., Rossi, V. & Savary, S. Simulation modelling of yield losses caused by wheat stem rust. *Plant Pathol.* **71**, 544–555 (2022).

25. Mahlein, A. K., Oerke, E. C., Steiner, U. & Dehne, H. W. Recent advances in sensing plant diseases for precision crop protection. *Eur. J. Plant Pathol.* **133**, 197–209 (2012).

26. Ma, H. *et al.* Integrating Early Growth Information to Monitor Winter Wheat Powdery Mildew Using Multi-Temporal Landsat-8 Imagery. *Sensors* **18**, 3290 (2018).

27. Yuan, L., Zhang, H., Zhang, Y., Xing, C. & Bao, Z. Feasibility assessment of multi-spectral satellite sensors in monitoring and discriminating wheat diseases and insects. *Optik (Stuttg).* **131**, 598–608 (2017).

28. Zheng, Q., Huang, W., Cui, X., Shi, Y. & Liu, L. New spectral index for detecting wheat yellow rust using sentinel-2 multispectral imagery. *Sensors* **18**, 868 (2018).

29. Ruan, C. *et al.* Prediction of Wheat Stripe Rust Occurrence with Time Series Sentinel-2 Images. *Agriculture* **11**, 1079 (2021).

30. Yuan, L. *et al.* Selection of Spectral Channels for Satellite Sensors in Monitoring Yellow Rust Disease of Winter Wheat. *Intelligent Automation and Soft Computing* **19**, 501–511 (2013).

31. Yuan, L. *et al.* Damage Mapping of Powdery Mildew in Winter Wheat with High-Resolution Satellite Image. *Remote Sens. (Basel).* **6**, 3611–3623 (2014).

32. Zhang, J. *et al.* Integrating remotely sensed and meteorological observations to forecast wheat powdery mildew at a regional scale. *IEEE J. Sel. Top. Appl. Earth Obs. Remote Sens.* **7**, 4328–4339 (2014).

33. Zheng, Q. *et al.* Integrating Spectral Information and Meteorological Data to Monitor Wheat Yellow Rust at a Regional Scale: A Case Study. *Remote Sens. (Basel).* **13**, 278 (2021).

34. Airbus. Pléiades Neo: Native 30cm High-Resolution Satellite Imagery. https://space-solutions.airbus.com/imagery/our-optical-and-radar-satellite-imagery/pleiades-neo/ (2025).

35. Planet Labs. Satellite Imagery Analytics | Planet. https://www.planet.com/products/satellite-imagery-of-earth/ (2025).

36. Zhang, C., Marzougui, A. & Sankaran, S. High-resolution satellite imagery applications in crop phenotyping: An overview. *Comput. Electron. Agric.* **175**, 105584 (2020).

37. King, J. *et al.* Wheat genetic resources have avoided disease pandemics, improved food security, and reduced environmental footprints: A review of historical impacts and future opportunities. *Glob. Chang. Biol.* **30**, e17440 (2024).

38. Tattaris, M., Reynolds, M. P. & Chapman, S. C. A direct comparison of remote sensing approaches for high-throughput phenotyping in plant breeding. *Front. Plant Sci.* **7**, 1131 (2016).

39. Sankaran, S., Quirós, J. J. & Miklas, P. N. Unmanned aerial system and satellite-based high resolution imagery for high-throughput phenotyping in dry bean. *Comput. Electron. Agric.* **165**, 104965 (2019).

40. Pinto, F., Zaman-Allah, M., Reynolds, M. & Schulthess, U. Satellite imagery for high-throughput phenotyping in breeding plots. *Front. Plant Sci.* **14**, 1114670 (2023).

41. Victor, B. *et al.* High-Throughput Plot-Level Quantitative Phenotyping Using Convolutional Neural Networks on Very High-Resolution Satellite Images. *Remote Sens. (Basel).* **16**, 282 (2024).

42. Blasch, G. *et al.* The potential of UAV and very high-resolution satellite imagery for yellow and stem rust detection and phenotyping in Ethiopia. *Sci. Rep.* **13**, 16768 (2023).

43. Chen, D., Shi, Y., Huang, W., Zhang, J. & Wu, K. Mapping wheat rust based on high spatial resolution satellite imagery. *Comput. Electron. Agric.* **152**, 109–116 (2018).

44. Liu, L. *et al.* A Disease Index for Efficiently Detecting Wheat Fusarium Head Blight Using Sentinel-2 Multispectral Imagery. *IEEE Access* **8**, 52181–52191 (2020).

45. Yuan, L., Pu, R., Zhang, J., Wang, J. & Yang, H. Using high spatial resolution satellite imagery for mapping powdery mildew at a regional scale. *Precis. Agric.* **17**, 332–348 (2016).

46. Yuan, L., Bao, Z., Zhang, H., Zhang, Y. & Liang, X. Habitat monitoring to evaluate crop disease and pest distributions based on multi-source satellite remote sensing imagery. *Optik (Stuttg).* **145**, 66–73 (2017).

47. Yuan, L. *et al.* Mapping of powdery mildew using multi-spectral HJ-CCD image in Beijing suburban area. *Optik (Stuttg).* **124**, 4734–4738 (2013).

48. Dutta, S., Singh, S. K. & Khullar, M. A Case Study on Forewarning of Yellow Rust Affected Areas on Wheat Crop Using Satellite Data. *Journal of the Indian Society of Remote Sensing* **42**, 335–342 (2014).

49. Pignatti, S. *et al.* Sino-EU Earth Observation Data to Support the Monitoring and Management of Agricultural Resources. *Remote Sens. (Basel).* **13**, (2021).

50. Ruan, C. *et al.* Integrating Remote Sensing and Meteorological Data to Predict Wheat Stripe Rust. *Remote Sens. (Basel).* **14**, 1221 (2022).

51. Jing, X. *et al.* Quantifying the effects of stripe rust disease on wheat canopy spectrum based on eliminating non-physiological stresses. *CROP JOURNAL* **10**, 1284–1291 (2022).

52. Khosrokhani, M. & Nasr, A. H. Applications of the remote sensing technology to detect and monitor the rust disease in the wheat – a literature review. *Geocarto Int.* **37**, 13268–13290 (2022).

53. Zhang, J. *et al.* Monitoring plant diseases and pests through remote sensing technology: A review. *Comput. Electron. Agric.* **165**, 104943 (2019).

54. Abdulridha, J. *et al.* Evaluation of Stem Rust Disease in Wheat Fields by Drone Hyperspectral Imaging. *Sensors (Switzerland)* **23**, 4154 (2023).

55. EIAR. Debre Zeit Agricultural Research Center – EIAR. http://www.eiar.gov.et/main-center-debrezeit/ (2024).

56. Hengl, T. *et al.* SoilGrids250m: Global gridded soil information based on machine learning. *PLoS One* **12**, e0169748 (2017).

57. QGIS Development Team. QGIS Geographic Information System. Open Source Geospatial Foundation Project. https://qgis.org/en/site/ (2023).

58. Seifu, A. E., Mekibib, F. & T., D. Performance and farmers selection criteria Evaluation of Improved Bread Wheat Varieties. *Afr. J. Agric. Res.* **13**, 2477–2498 (2018).

59. Hodson, D. P. *et al.* Ethiopia's transforming wheat landscape: tracking variety use through DNA fingerprinting. *Scientific Reports 2020 10:1* **10**, 1–13 (2020).

60. Kidane Alemu, S. *et al.* Identification of Stem Rust Resistance Genes in Released Wheat Varieties by Linked SSR Markers and Phenotypic Screening. *Article in International Journal of Genetics and Genomics* **11**, 48–59 (2023).

61. Degife, G. & Demis, E. Performance Evaluation of Improved Bread Wheat (Triticum aestivum L.) Varieties at Southern Tigray, Northern Ethiopia. *Global Scientific Journals* **9**, 626–636 (2021).

62. CIMMYT. *Yield and Yield Components - A Practical Guide for Comparing Crop Management Practices*. (CIMMYT, Texcoco, Mexico, 2013).

63. Peterson, R. F., Campbell, A. B. & Hannah, A. E. A DIAGRAMMATIC SCALE FOR ESTIMATING RUST INTENSITY ON LEAVES AND STEMS OF CEREALS. *Can. J. Res.* **26c**, 496–500 (1948).

64. CIMMYT. *Rust Scoring Guide*. (CIMMYT, Mexico City, Mexico, 1986).

65. Roelfs, A. P., Singh, R. P. & Saari, E. E. *Rust Diseases of Wheat: Concepts and Methods of Disease Management*. (CIMMYT, 1992).

66. Coeurdevey, L. & Fernandez, K. *Pléiades Imagery - User Guide*. (Airbus Defence and Space Intelligence, France, 2012).

67. Liu, P., Xiao, L. & Li, T. A Variational Pan-Sharpening Method Based on Spatial Fractional-Order Geometry and Spectral-Spatial Low-Rank Priors. *IEEE Transactions on Geoscience and Remote Sensing* **56**, 1788–1802 (2018).

68. Alcaras, E., Parente, C. & Vallario, A. Automation of Pan-Sharpening Methods for Pléiades Images Using GIS Basic Functions. *Remote Sens. (Basel).* **13**, 1550 (2021).

69. Rodrigues, F. A. *et al.* Multi-temporal and spectral analysis of high-resolution hyperspectral airborne imagery for precision agriculture: Assessment of wheat grain yield and grain protein content. *Remote Sens. (Basel).* **10**, 930 (2018).

70. Inoue, Y., Sakaiya, E., Zhu, Y. & Takahashi, W. Diagnostic mapping of canopy nitrogen content in rice based on hyperspectral measurements. *Remote Sens. Environ.* **126**, 210–221 (2012).

71. Inoue, Y., Peñuelas, J., Miyata, A. & Mano, M. Normalized difference spectral indices for estimating photosynthetic efficiency and capacity at a canopy scale derived from hyperspectral and CO2 flux measurements in rice. *Remote Sens. Environ.* **112**, 156–172 (2008).

72. Inoue, Y. *et al.* Simple and robust methods for remote sensing of canopy chlorophyll content: a comparative analysis of hyperspectral data for different types of vegetation. *Plant Cell Environ.* **39**, 2609–2623 (2016).

73. Inoue, Y. *et al.* NDSI Map and IPLS Using Hyperspectral Data for Assessment of Plant and Ecosystem Variables —With a Case Study on Remote Sensing of Grain Protein Content, Chlorophyll Content and Biomass in Rice—. *Journal of The Remote Sensing Society of Japan* **28**, 317–330 (2008).

74. Stratoulias, D., Balzter, H., Zlinszky, A. & Tóth, V. R. Assessment of ecophysiology of lake shore reed vegetation based on chlorophyll fluorescence, field spectroscopy and hyperspectral airborne imagery. *Remote Sens. Environ.* **157**, 72–84 (2015).

75. Stagakis, S., Markos, N., Sykioti, O. & Kyparissis, A. Monitoring canopy biophysical and biochemical parameters in ecosystem scale using satellite hyperspectral imagery: An application on a Phlomis fruticosa Mediterranean ecosystem using multiangular CHRIS/PROBA observations. *Remote Sens. Environ.* **114**, 977–994 (2010).

76. Vanderplank, J. E. *Plant Diseases: Epidemics and Control.* (Academic Press, New York, 1963).

77. R Core Team. R: The R Project for Statistical Computing. https://www.r-project.org/ (2022).

78. Rehman, S. ur *et al.* Exploring the Frontier of Wheat Rust Resistance: Latest Approaches, Mechanisms, and Novel Insights. *Plants (Basel).* **13**, 2502 (2024).

79. Launay, M. *et al.* Climatic indicators for crop infection risk: Application to climate change impacts on five major foliar fungal diseases in Northern France. *Agric. Ecosyst. Environ.* **197**, 147–158 (2014).

80. Kingsolver, C. H., Schmitt, C. G., Peet, C. E. & Bromfield, K. R. Epidemiology of stem rust II. Relation of quantity of inoculum and growth stage of wheat and rye at infection to yield reduction by stem rust. *Plant Disease Reporter* **43**, 855–862 (1959).

81. Silva, J. V. *et al.* Pathways to wheat self-sufficiency in Africa. *Glob. Food Sec.* **37**, 100684 (2023).

82. Shakoor, N., Lee, S. & Mockler, T. C. High throughput phenotyping to accelerate crop breeding and monitoring of diseases in the field. *Curr. Opin. Plant Biol.* **38**, 184–192 (2017).

83. Ali, M. M., Bachik, N. A., Muhadi, N. ‘Atirah, Tuan Yusof, T. N. & Gomes, C. Non-destructive techniques of detecting plant diseases: A review. *Physiol. Mol. Plant Pathol.* **108**, 101426 (2019).

84. Simko, I., Jimenez-Berni, J. A. & Sirault, X. R. R. Phenomic Approaches and Tools for Phytopathologists. *Phytopathology* **107**, 6–17 (2017).

85. Thomas, S. *et al.* Benefits of hyperspectral imaging for plant disease detection and plant protection: a technical perspective. *Journal of Plant Diseases and Protection* **125**, 5–20 (2018).

86. Zhang, N. *et al.* A review of advanced technologies and development for hyperspectral-based plant disease detection in the past three decades. *Remote Sens. (Basel).* **12**, 1–34 (2020).

87. Zhang, J. *et al.* Monitoring Powdery Mildew of Winter Wheat by Using Moderate Resolution Multi-Temporal Satellite Imagery. *PLoS One* **9**, e93107 (2014).

88. Sims, D. A. & Gamon, J. A. Relationships between leaf pigment content and spectral reflectance across a wide range of species, leaf structures and developmental stages. *Remote Sens. Environ.* **81**, 337–354 (2002).

89. Wu, C., Niu, Z., Tang, Q. & Huang, W. Estimating chlorophyll content from hyperspectral vegetation indices: Modeling and validation. *Agric. For. Meteorol.* **148**, 1230–1241 (2008).

90. Fedotov, A., Eremenko, D., Kuznetsova, D., Baranova, O. & Terentev, A. Advanced hyperspectral image processing and machine learning approaches for early detection of wheat stem rust. *Front. Plant Sci.* **16**, 1725017 (2025).

91. Lee, D.-Y. & Na, D.-Y. Full-Wave Optical Modeling of Leaf Internal Light Scattering for Early-Stage Fungal Disease Detection. *Agriculture 2026, Vol. 16,* **16**, 286 (2026).

92. Arya, G. C., Sarkar, S., Manasherova, E., Aharoni, A. & Cohen, H. The Plant Cuticle: An Ancient Guardian Barrier Set Against Long-Standing Rivals. *Front. Plant Sci.* **12**, 663165 (2021).

93. Wan, L. ; *et al.* Hyperspectral Sensing of Plant Diseases: Principle and Methods. *Agronomy* **12**, 1451 (2022).

94. Oerke, E. C. Remote Sensing of Diseases. *Annual Review Phytopathology* **58**, 225–252 (2020).

95. Khaled, A. Y. *et al.* Early detection of diseases in plant tissue using spectroscopy – applications and limitations. *Appl. Spectrosc. Rev.* **53**, 36–64 (2018).

Acknowledgments

We greatly acknowledge the support of partnering institutions and financial support for the study through the CGIAR Initiative on Plant Health. Additional support through the Disease Early Warning Advisory System-Wheat (DEWAS – INV048345) project funded by the Gates Foundation and the United Kingdom Foreign & Commonwealth Development Office (FCDO) is greatly acknowledged. Moreover, staff at EIAR Debre Zeit Research Center are greatly acknowledged for establishing and managing the field experiment. We thank the European Space Agency (ESA), Planet Labs, and the Université catholique de Louvain (Prof. Pierre Defourny) for providing the Pleiades-Neo and SkySat data, in the context of the Sentinel For Wheat Rust Disease (SEN4RUST) project, through the ESA's Third-Party Mission scheme – Data provided by the European Space Agency.

Funding

We greatly acknowledge the support of partnering institutions and financial support for the study through the CGIAR Initiative on Plant Health. Additional support through the Disease Early Warning Advisory System-Wheat (DEWAS – INV048345) project funded by the Gates Foundation and the United Kingdom Foreign & Commonwealth Development Office (FCDO) is greatly acknowledged. Moreover, staff at EIAR Debre Zeit Research Center are greatly acknowledged for establishing and managing the field experiment. We thank the European Space Agency (ESA), Planet Labs, and the Université catholique de Louvain (Prof. Pierre Defourny) for providing the Pleiades-Neo and SkySat data, in the context of the Sentinel For Wheat Rust Disease (SEN4RUST) project, through the ESA's Third-Party Mission scheme – Data provided by the European Space Agency.

Author information

Authors and Affiliations

International Maize and Wheat Improvement Center (CIMMYT), Texcoco, Mexico
Gerald Blasch

Debre Zeit Agricultural Research Center (DZARC), Debre Zeit, Ethiopia
Ashenafi Gemechu

International Maize and Wheat Improvement Center (CIMMYT), Addis Ababa, Ethiopia
Yoseph Alemayehu; Adama Ndour

United States Department of Agriculture, St. Paul, MN, United States
Pablo Olivera Firpo

University of Queensland, Brisbane, Australia
Andries Potgieter

International Maize and Wheat Improvement Center (CIMMYT), Kathmandu, Nepal
David P. Hodson

Contributions

G.B.: Project conceptualization, design, coordination, and supervision, methodology, satellite data acquisition and processing, investigation, data analytics conceptualization, data analysis and visualization, writing - original draft, review and editing, funding acquisition. A.G.: Experiment set up, methodology, field data collection, investigation, writing - review and editing. Y.A.: Project co-coordination, methodology, investigation, writing - review and editing. A.N., P.O.F., A.P.: Writing - review and editing. D.P.H.: Project conceptualization, writing - review and editing, funding acquisition.

Corresponding author

Correspondence to Gerald Blasch.

Data availability

Remote sensing data from Pleiades-Neo and SkySat were provided through the European Space Agency's Third-Party Mission scheme (ESA TPM). All other data that support the findings of this study are available from the corresponding author upon reasonable request.

Ethics declarations

Competing interests

The authors declare no competing interests.

Additional information

Supplementary Files

This is a list of supplementary files associated with this preprint. Click to download.

- ManuscriptDZARC2023v7supplMaterialrd1.docx